



HAL
open science

Multi-scale analysis of atomizing liquid ligaments

Christophe Dumouchel, Jean-Bernard Blaisot, Emmanuella Bouche, Thibaut
Ménard, Trung-Thanh Vu

► **To cite this version:**

Christophe Dumouchel, Jean-Bernard Blaisot, Emmanuella Bouche, Thibaut Ménard, Trung-Thanh Vu. Multi-scale analysis of atomizing liquid ligaments. *International Journal of Multiphase Flow*, 2015, 73, pp.251–263. 10.1016/j.ijmultiphaseflow.2015.03.020 . hal-01612376

HAL Id: hal-01612376

<https://hal.science/hal-01612376v1>

Submitted on 29 Jul 2024

HAL is a multi-disciplinary open access archive for the deposit and dissemination of scientific research documents, whether they are published or not. The documents may come from teaching and research institutions in France or abroad, or from public or private research centers.

L'archive ouverte pluridisciplinaire **HAL**, est destinée au dépôt et à la diffusion de documents scientifiques de niveau recherche, publiés ou non, émanant des établissements d'enseignement et de recherche français ou étrangers, des laboratoires publics ou privés.

Multi-Scale Analysis of Atomizing Liquid Ligaments

Christophe Dumouchel¹, Jean-Bernard Blaisot, Emmanuella Bouche, Thibaut Ménard,
Trung-Thanh Vu

CNRS UMR 6614 – CORIA

Université et INSA de Rouen, B.P. 12

76801 Saint Etienne du Rouvray, France

Abstract

The atomization of individual liquid ligaments appearing during the disintegration of liquid sheets issuing from a triple-disk injector is investigated. High-speed visualizations report a temporal evolution of the ligaments from their production to their disintegration into drops. The parameter of the experiments is the surface tension of the liquid. A multi-scale analysis consisting in describing the temporal evolution of the ligament shape by measuring the scale-distribution is performed. This analysis introduces the notion of scale-diameter whose temporal variation leads to the following conclusion. The ligaments are subject to elongation, capillary deformation and break up and relaxation mechanisms. These mechanisms appear concomitantly on different scales. This concomitancy depends on the surface tension, i.e., on a Weber number based on the ligament initial elongation rate and initial size: the decrease of the surface tension favor the propensity of the atomization process to cascade in the scale space towards the small scale region. A mathematical scale-distribution of the final drops is

¹ Corresponding Author: christophe.dumouchel@coria.fr, Tel: +33 (0)2 32 95 36 23, Fax: +33 (0)2 32 91 04 85

satisfactorily derived from an atomization model of the literature. Furthermore, the parameters introduced by this model are well correlated to initial ligament Weber number and size.

Keywords

Liquid ligament, atomization, multi-scale analysis, shape analysis

1. Introduction

Ligamentary structures are often encountered in liquid atomization processes. In 1962, Fraser et al. suggest that the atomization of liquid sheets subject to a Kelvin-Helmholtz instability goes through the production of transverse ligaments that disintegrate in droplets following a capillary instability mechanism. Since then, many experimental images of atomization processes have revealed the presence of ligaments before the final drop production stage. For instance, under sub-atmospheric pressure, liquid sheets perforate and rearrange as a ligament network before producing drops (Fraser et al. 1962). Liquid sheets surrounded by a high velocity gas-flow may disintegrate under a cellular regime characterized by the production of ligaments (Lozano et al., 1996). The perforation atomization regime observed on conical high-viscous liquid sheets produces ligaments (Sindayihebura and Dumouchel, 2001). Radial liquid sheets in the sinusoidal regime of instability reorganize as longitudinal ligaments at their edge before the drop production stage (Clanet and Villermaux, 2002). Air-assisted cylindrical liquid jets subject to a Rayleigh-Taylor instability generate longitudinal ligaments as the next to the last step of the atomization process (Marmottant and Villermaux, 2004a). Finally, liquid sheets produced by the impact of two jets reorganize as a succession of transverse ligaments that to their turn disintegrate as droplets (Brémond and Villermaux, 2006). In every situation the final spray characteristics depend on the atomization of the ligaments that therefore deserves targeted investigations. This work is dedicated to the breakup of such ligaments but not to their production.

The liquid ligaments considered in this study are those appearing during the atomization process of flows issuing from a triple-disk nozzle. The working principle of triple-disk nozzles was investigated in previous works (Dumouchel et al., 2005a, 2005b). Inspired

from compound port fuel injector, a triple-disk nozzle is made of the superposition of three disks, the nozzle discharge orifice in the third disk being not aligned with the passages in the two other disks. Because of this geometrical characteristic, the liquid flow issuing from the nozzle is shaped as a 2D sheet. The atomization process of this sheet is initiated by the liquid turbulence and goes through the creation of gulfs, the reorganisation as a ligament network and the subsequent breakup of these ligaments into droplets. The last stage of this process is investigated here.

A cylindrical liquid ligament is naturally meant to breakup into droplets. It is subjected to an instability driven by capillary forces and whose growth leads to its breakup and the production of droplets. The first-order (or linear) theoretical description of this instability due to Rayleigh (1878) provides the instability wavelength λ ($= 4.51D_L$ where D_L is the ligament initial diameter) and its characteristic capillary time t_σ ($= \sqrt{\rho_L D_L^3 / \sigma}$ where ρ_L is the liquid density and σ the surface tension). The diameter D_G of the droplets produced by this mechanism can be estimated by considering that one drop is produced per wavelength. It comes $D_G = 189D$. Third order mathematical developments (Yuen, 1968; Rutland and Jameson, 1970) showed that the capillary instability is a non-linear effect with generation of higher harmonics, feedback into the fundamental and production of swelling between the crests of primary disturbance waves. Pimbley and Lee (1977) demonstrated that this non-linear effect is at the origin of satellite drops, i.e., smaller drops produced between two first-order droplets. The most relevant parameters that control the production of satellite drops are the amplitude of the perturbation and the wavelength-to-diameter ratio of this perturbation. The direct numerical simulation of ligament capillary instability performed by Ashgriz and Mashayek (1995) demonstrates that the satellite production depends on the jet

Ohnesorge number Oh ($= \mu / \sqrt{\rho_L \sigma D_L}$ where μ is the liquid dynamic viscosity) and on the disturbance wavenumber k and initial amplitude. They succeed in identifying the satellite production region in the $(k, 1/Oh)$ domain and found that the satellite might disappear when the disturbance initial amplitude increases.

Frankel and Weihs theoretically investigated the effect of an elongation constraint on the instability of jets of non-viscous (1985) and viscous (1987) liquids. Their works demonstrate that the evolution of surface perturbations in the jet is an initial value problem instead of an eigenvalue one. Perturbation amplification depends on the relative effects of the surface tension and inertia terms associated with extensional flow. It depends also on the initial wavelength and on the specific time when the perturbation is introduced in the flow. In the case of viscous liquid, the ligament behavior depends on three characteristic times, i.e., the elongation characteristic time t_e ($= 1/\alpha$ where α is the elongation rate), the capillary characteristic time t_σ and the vorticity diffusion characteristic time t_μ ($= \rho_L D_L^2 / \mu$).

Stretched ligaments were experimentally investigated by Marmottant and Villermaux (2004b). When the ratio $t_\sigma/t_e \gg 1$, the elongation is rapid and the ligament elongates as a liquid column. This column eventually breaks into droplets. Contrary to the Rayleigh instability mechanism, the drops produced here have different sizes. This was explained by several mechanisms such as the capillary wave travel along the ligament, the transient growth of the capillary instability and the remnant motions in the liquid bulk. The second argument was theoretically evidenced by Frankel and Weihs (1985). Marmottant and Villermaux (2004b) paid a specific attention to the set of droplets after breakup. They found that the mean diameter D_{10} was of the order of twice the ligament diameter just before breakup occurs. Furthermore, the mathematical diameter

distribution they established from a fragmentation model based on successive agglomerations of sub-blobs satisfactorily fitted the measured diameter distributions. This latter result was also found for droplets produced from Rayleigh-Taylor ligament atomization (Marmottant and Villermaux, 2004a).

The numerical investigation due to Tong and Wang (2007) highlights that elongated ligaments are not all meant to break into several drops. Under certain conditions, an elongated ligament can relax into a single drop. This behavior is due to a competition between opposite internal flows in the region of a neck deformation. This one-drop relaxation mechanism is enhanced when the ligament Ohnesorge number Oh is great or for pointed-ends ligaments. In a liquid atomization process, such a mechanism may be expected on liquid bridges between two main drops since they have a small diameter (i.e., great Oh) and may have pointed-ends if the motion of the two main drops imposes an elongation constraint.

The purpose of this work is to investigate the atomization mechanisms of ligaments emanating from the disintegration of 2D liquid sheets produced by a triple-disk nozzle. To achieve this, a high-speed camera is used to record ligament temporal evolutions. The subsequent analysis is based on the description of the shapes of the ligaments during time. Liquid ligaments emanating from atomization processes exhibit complex shapes and specific tools are required here. The question of shape characterization of disintegrating liquid systems has been addressed since the mid 90's (refer to the review paper of Dumouchel, 2008). Attempts of using the fractal dimension concept were conducted and revealed that atomizing liquid systems have fractal characteristics but that these characteristics do not provide a complete description of the system. Inspired from the fractal description, a multi-scale analysis has been established and applied to

describe liquid sprays (Dumouchel et al. 2008) or a liquid atomization process (Dumouchel and Grout, 2009). This latter work shows also that a new modeling of liquid atomization processes can be based on the multi-scale description. The multi-scale analysis is used here. It is the first time it is applied on temporally resolved atomization process and the evaluation of its potential in such a situation constitutes another aim of the work.

The article contains three main sections. The experimental work is described in Section 2; the multi-scale description tools are presented in Section 3, and the experimental results and analysis are shown and discussed in Section 4.

2. Experimental Work

The experimental setup is conceived to produce liquid sprays at low injection pressures under atmospheric conditions of temperature and pressure. The liquid is kept in a pressurized tank and filtered before reaching the injector. A single injector is used. It has a triple-disk nozzle as schematized in Fig. 1. This nozzle is constituted of the superposition of three circular disks. The liquid enters the nozzle through disk 1, flows through the cavity disk (disk 2) and discharges through the single orifice in disk 3. The drastic flow deflections imposed by the nozzle eccentricity (see Fig. 1) favors the development of a remarkable flow at the nozzle exit section: it shows a double counter-rotating swirl as well as a consistent turbulent level (Dumouchel et al., 2005a). As soon as the liquid issues from the nozzle, the double swirl stretches the flow in the x -direction and the issuing liquid flow takes the form of a 2D sheet in the $(0; x; z)$ plane. The turbulence induces initial perturbations on the sheet edges. Some of them grow and constraint the flow to reorganize as a ligament network that eventually breaks into

droplets. The geometrical dimensions of the triple-disk nozzle used in the present work are given in Table 1. An example of the liquid flow issuing from this nozzle is shown in Fig. 2 (Liquid: water, injection pressure: 0.1 MPa). The flow is stretched in the image plane to form a liquid sheet that is not symmetric because of the non-symmetry of the nozzle geometry. The deformation of this sheet induces the production of span-wise ligaments on its right side, i.e., towards the center of the nozzle (see Fig. 1). The experimental work focused on the temporal behavior of these ligaments. A high-speed camera (Phantom V12) was used in a shadowgraph configuration for this purpose. The frame rate was set to 25,000 frames/s, allowing a good tradeoff between temporal resolution (image interval = 40 μ s) and image definition (640 x 352 pixels). The visualization field (3.5 mm x 6.4 mm) corresponds to a spatial resolution of 10.36 μ m/pixel and was positioned in the ligament network region. The light source was a mono-chromatic non-coherent laser diode source (Cavitar Cavilux HF) associated with a collimation optic to produce a slightly divergent speckle-free laser beam. This source is characterized by a very good temporal and spatial stability, which makes it particularly appropriate to perform high quality shadowgraph images as those shown in Fig. 3.

The spatial and temporal descriptions are improved if the ligaments are thick and slow. For this reason the injection pressure, measured just upstream the nozzle is maintained at a constant low value equal to 0.1 MPa. Three different liquids are used. They are identified by capital letters, i.e., Liquid A: water; Liquid B: a water-ethanol 10% mixture; and Liquid C: a water-ethanol 15% mixture. Their physical properties are given in Table 2. For every liquid, the mass-flux average velocity V_q at the nozzle exit is of the order of 7 m/s for the injection pressure equal to 0.1 MPa.

Individual ligament sequences were identified on the high-speed films. Figure 3 shows an example of such a sequence (Liquid C). In this figure, only one image over two is shown, i.e., the temporal gap between two consecutive images is 80 μ s. In the four first images, the ligament is still attached to the bulk flow. This situation was frequent and the analysis had to begin with the manual determination of the location of separation from the bulk flow. The arrow in Fig. 3 shows where the separation was performed. In the first times, this step may introduce a slight inaccuracy on the system definition. For each liquid, three individual ligament temporal evolutions were identified. They are numbered 1 to 3. In the following, the ligaments are identified by LXY where X is the liquid letter and Y the ligament number.

The image analysis applied to derive the ligament contour comprises three steps, namely, normalization, segmentation and contour identification. Normalization is a pre-treatment step whose objective is to fix spatial and temporal variability in the background image. The second step, segmentation, combines an application of a continuous wavelet transform to identify small gray-level variations typical for small or out-of-focus objects, and a global-image thresholding in order to detect large objects characterized by low gray-level values. The third step uses object identified at the previous step and does a local analysis of this object and its direct surrounding. The local gray-level threshold used to compute the object contour is determined from an imaging model based on point-spread-function formalism (Fdida and Blaisot, 2010). In the present case, contour detection with pixel resolution is used because the multi-scale analysis implies pixel-based morphological operations. Typical results are shown in Figure 4, namely, LA1 (left), LB2 (center) and LC3 (right). (For clarity's sake, only one event over two is shown in this figure for LB2. For this ligament, the time gap between

two consecutive events is 80 μ s.) These examples show that the initial ligament shape is very different from one situation to another. Let us add that, for every liquid, the three ligaments report very different initial shapes. However they exhibit similar behaviors that depend on the surface tension. First, a continuous and constant span-wise expansion is visible at all times, i.e., from the initial ligament stage to the drop stage. This expansion increases as the surface tension decreases. Second, the small droplets are more numerous when the surface tension decreases. For liquids B and C, small droplets emanate from the breakup of secondary ligaments produced by the detachment of small liquid bridges stretched between larger liquid structures. These behaviors are visible in Fig. 4 as well as on the other ligaments not shown here.

These observations demonstrate that the ligament evolution involves several mechanisms. The span-wise expansion pleads to the presence of an elongation mechanism. The production of the large drops is associated to the capillary deformation and breakup mechanism similar to the Rayleigh mechanism (see Introduction). Finally, the production of the small droplets identified for LB and LC is due to the breakup of stretched secondary ligaments. Adopting the Tong and Wang's terminology (Tong and Wang, 2007), this mechanism is referred in the following as the relaxation mechanism.

By analyzing the temporal evolution of the shape of the ligaments, we intend to identify and characterize the contribution of these three mechanisms referred here after as 1 – Elongation, 2 – Capillary deformation and breakup, 3 – Relaxation. To achieve this, and because the encountered shapes are complex, we apply the multi-scale analysis used in several previous studies (Dumouchel et al., 2008; Dumouchel and Grout, 2009) and summarized in the next section.

3. The Multi-Scale description tools

The multi-scale analysis was introduced to characterize liquid sprays (Dumouchel et al., 2008) and was successfully applied to describe the atomization process of liquid sheets produced by a triple-disk nozzle (Dumouchel and Grout, 2009). It is based on the measurement of the cumulative function $E_2(d)$ where the variable d is the scale of observation. Let us consider a system of any shape as the one shown in Fig. 5-a for instance. This system has a surface noted S_T (gray area in Fig. 5-a). The system is eroded by circular structuring elements of various diameters d . For each erosion step, i.e., for each value of d , the remaining surface $S(d)$ (the white surface delimited by the dash line in Fig. 5-b) is measured. The cumulative scale function is defined by:

$$E_2(d) = \frac{S_T - S(d)}{S_T} \quad (1)$$

When d varies from 0 to infinity, $E_2(d)$ monotonously increases from 0 to 1. This function is the cumulative scale function. Adopting the formalism traditionally in use for diameter distributions, we consider the first derivative of the cumulative distribution in the space scale, introducing the scale distribution $e_2(d)$:

$$e_2(d) = \frac{dE_2(d)}{dd} \quad (2)$$

The dimension of $e_2(d)$ is the inverse of a length. This function expresses the ratio of the perimeter of the eroded system at scale d (length of the dash line in Fig. 5-b) on twice the total surface S_T . For $d = 0$, this is proportional to the interface length per unit surface

which is an important quantity in atomization. Since the perimeter of the eroded system at scale d always decreases as the scale increases, the scale distribution is a monotonously decreasing function and has a maximum at $d = 0$.

In this formalism, any system is described by the scale dependent functions $E_2(d)$ and $e_2(d)$. For instance, the scale distribution of a circle of diameter D is linearly dependent on the scale (Dumouchel et al. 2008). It writes:

$$e_2(d) = \frac{2}{D} \left(1 - \frac{d}{D} \right) \quad (3)$$

The functions $E_2(d)$ and $e_2(d)$ are shape dependent. However, systems with different shapes may have the same cumulative scale function and scale distribution. Such systems would have the same perimeter to total surface ratio at all scales d . In particular, they would have the same amount of interface per unit surface. The scale distribution is not a measurement of the shape but a measurement of the contour length density as a function of the scale. This information is believed to be more important in atomization than the shape itself. The fact several systems may have the same scale distribution has been used to introduce the notion of equivalent systems (Dumouchel and Blaisot, 2013). This concept will be used at the end of this work.

In the present work, the scale distribution is a function of time and writes $e_2(d,t)$. As shown and discussed in the next section, the temporal variation of the scale distribution induced by the shape evolution of the ligaments is often slight. In order to recover sensitivity from the measurements, we suggest considering the inverse of the scale distribution. This new quantity is equivalent to a length. It is called the scale-diameter and is noted $D(d,t)$:

$$D(d,t) = \frac{1}{e_2(d,t)} \quad (4)$$

The scale-diameter can be seen as the width of the rectangle whose height is equal to half the perimeter of the eroded system at scale d and whose surface is equal to S_T .

Besides the scale-diameter, the analysis also considers the temporal derivate of the scale distribution introducing the function $\beta(d,t)$:

$$\beta(d,t) = \frac{de_2(d,t)}{dt} \quad (5)$$

$\beta(d,t)$ can be expressed as a function of the scale-diameter (Eq. (4)). It comes:

$$\beta(d,t) = -\frac{1}{D(d,t)^2} \frac{dD(d,t)}{dt} \quad (6)$$

For a stretched liquid cylinder of volume V , it is easy to show that the rate of surface variation per unit volume depends on the column diameter $D(t)$ as:

$$\frac{1}{V} \frac{dS(t)}{dt} \propto -\frac{1}{D(t)^2} \frac{dD(t)}{dt} \quad (7)$$

Comparing Eqs. (6) and (7) shows that the function $\beta(d,t)$ can be seen as an indicator of the surface variation rate per unit volume. For $d=0$, the surface is the one of the

system. For other scales, the surface is fictive; it is the one of the eroded system at the corresponding scale.

As examples and in order to help interpreting the results of the analysis, the functions $D(d,t)$ and $\beta(d,t)$ are established for the elongation, the capillary deformation and breakup and the relaxation mechanisms introduced in the previous section. Initial and final stages of these mechanisms are considered only. Their 2D perceptions are simplified as shown in Fig.6.

Description of mechanism 1: the elongation

In 2D, the elongation of a cylinder is represented by a rectangle with an initial width (or diameter) $D_j(t_i)$ that becomes a rectangle of final width (or diameter) $D_j(t_f)$. The volume conservation imposes that, at any time, the rectangle surface $S(t) = 4V/\pi D_j(t)$ where V is the volume of the cylinder. It is straightforward to show that at any time $e_2(d,t) = 1/D_j(t)$ and therefore that:

$$\begin{cases} D(d,t) = D_j(t) \\ \beta(d,t) = -\frac{1}{D_j(t)^2} \frac{dD_j(t)}{dt} \end{cases} \quad (8)$$

The elongation mechanism is a specific case for which all functions lose their dependence with the scale d . This is due to the fact that the curvature of the 2D projected-system boundary is everywhere and always equal to zero. On the other hand, for complex shapes, these functions become scale dependent through a quantitative sensitivity to non-zero boundary curvature characteristics.

For a positive elongation process as schematized in Fig. 6, $D_j(t)$ decreases with time and Eq. (8) indicates a negative temporal derivative for $D(d,t)$ and a positive function $\beta(d,t)$.

Description of mechanism 2: the capillary deformation and breakup

In 2D, the initial stage of this mechanism is represented by a rectangle with a width (or diameter) equal to D_j and a length equal to $4.51D_j$ and the final stage is a circle with a diameter equal to $D_G = 1.89D_j$. For these shapes, it is straightforward to calculate the scale distributions $e_2(d)$ and to deduce the initial and final scale-diameter functions. It comes:

$$\begin{cases} D(d, t_i) = D_j \\ D(d, t_f) = \frac{1.89D_j}{2 \left(1 - \frac{d}{1.89D_j} \right)} \end{cases} \quad (9)$$

Equation (9) reveals that for $d \in [0; 0.1D_j]$, $D(d,t)$ decreases slightly between t_i and t_f . The maximum amplitude of decrease is obtained for $d = 0$ and is equal to $0.055D_j$. On the other hand, for $d \in [0.1D_j, D_j]$ $D(d,t)$ increases with time and the greater the scale d is, the greater the scale-diameter increase. (Note that for $d > D_j$, the reasoning cannot be conducted anymore since these scales don't exist at initial time.) Therefore, the capillary deformation and breakup mechanism has the following scale-diameter characteristics:

$$\begin{cases} \text{For } d \in [0; 0.1D_j] & \frac{dD(d,t)}{dt} < \approx 0 \\ \text{For } d \in [0.1D_j; D_j] & \frac{dD(d,t)}{dt} > 0 \end{cases} \quad (10)$$

As shown by Eq. (6), the corresponding function $\beta(d,t)$ has the opposite sign.

Description of mechanism 3: the relaxation

As for the previous mechanism, the initial stage of the relaxation is represented in 2D by a rectangle and the final stage by a circle. The dimensions of the rectangle are D_G/x and H and the diameter of the circle is D_G . In this presentation, the number x is a parameter. By volume conservation, it is easy to show that $H = 2D_Gx^2/3$. The case $x = 1.89$ exactly corresponds to the capillary deformation and breakup mechanism described above. The relaxation mechanism intends to represent the possible behavior of thin ligaments i.e. those for which x is greater than 2 at least. The initial and final scale-diameter functions are equal to:

$$\left\{ \begin{array}{l} D(d, t_i) = \frac{D_G}{x} \\ D(d, t_f) = \frac{D_G}{2\left(1 - \frac{d}{D_G}\right)} \end{array} \right. \quad (11)$$

For $x > 2$, Eq. (11) highlights an increase of the scale-diameter for all scales. Therefore, the relaxation mechanism is characterized by a positive temporal derivate of the scale-diameter for all scales. The corresponding function $\beta(d,t)$ is negative.

By using the scale-diameter description it is possible to show that the breakup of the stretched ligaments investigated by Marmottant and Villermaux (2004b) falls within the relaxation mechanism. The number-based diameter distribution $f_0(D)$ of the drops

produced by these ligaments was found to be well represented by a gamma distribution of order ν , i.e.:

$$f_0(D) = \frac{\nu^\nu}{\Gamma(\nu)} \frac{D^{\nu-1}}{D_{10}^\nu} \exp\left(-\nu \frac{D}{D_{10}}\right) \quad (12)$$

where $\Gamma(x)$ is the gamma function, D is the drop diameter variable and D_{10} is a diameter of the mean-diameter series D_{mn} standardized by Mugele and Evans (1957). For the diameter distribution given by Eq. (12), this mean-diameter series can be expressed as a function of the order ν and the mean diameter D_{10} . It comes:

$$D_{mn} = \frac{1}{\nu} \left(\frac{\Gamma(\nu + m)}{\Gamma(\nu + n)} \right)^{1/(m-n)} D_{10} \quad (13)$$

where m and n can be any reals provided that they are different.

Marmottant and Villermaux (2004a) found an order ν ranging from 2.6 to 8.1. Using Eq. (13) this interval of ν corresponds to a ratio (D_{21}/D_{10}) ranging from 1.12 to 1.4. Furthermore, they also noted that the ratio D_{10}/D_L , where D_L represents the ligament diameter just before break-up, was of the order of 2. Considering that the initial stage of the system is a cylindrical column with a diameter D_L , the corresponding scale-diameter at scale $d = 0$ is $D(0, t_i) = D_L$. The final stage is a set of spherical elements whose diameters are distributed according to Eq. (12). For such system, it has been shown that $e_2(0) = 2/D_{21}$ (Dumouchel et al., 2008). Therefore, the final stage scale-diameter at $d = 0$ is $D(0, t_f) = D_{21}/2$. All this information leads to:

$$1.12 \leq \frac{D(0, t_f)}{D(0, t_i)} \leq 1.4 \quad (14)$$

This equation reports a temporal increase of the scale-diameter at scale $d = 0$ as found for the relaxation mechanism.

We see that the temporal evolution of the scale-diameter function allows identifying mechanisms acting on the system at a given instant. For instance, the information for the scale $d = 0$, i.e., at the interface, clearly discriminates the three mechanisms since the corresponding scale-diameter temporal derivative is negative, equal to zero or positive for the elongation, the capillary deformation and breakup, and the relaxation mechanisms, respectively.

The accuracy of the $E_2(d)$ measurement procedure is evaluated by performing a measurement on a synthetic image. This image contains circles of identical diameter for which the scale distribution is theoretically known (Eq. (3)). In order to work with an image representative of the experimental ones, the total surface of the circles should be of the same order as the surface of the ligaments and the circle diameter should be of the same order as the largest experimental scale. These considerations led to a synthetic image with 10 circles of 20 pixels diameter. The circles were randomly positioned in the image. The cumulative scale function $E_2(d)$ is measured using ImageJ software and the $e_2(d)$ is calculated using a centered derivative formulation. Two situations are tested: 1 – $e_2(d)$ is calculated from the raw $E_2(d)$ values; 2 – A 3-point local mean of $E_2(d)$ is performed before the calculation of $e_2(d)$ in order to smooth the high-frequency variations of the measurements. The calculated and theoretical scale distributions are

shown in Fig. 7. We see that the scale distribution calculated with the smoothed cumulative values agrees very well with the theoretical one. The error is less than 1% over the entire scale range except at the largest scale (20 pixels) where it is of the order of 4%. This loss of accuracy is due to the smoothing and derivative calculation procedures that both spread the scale distribution variations. Anyway, the result remains very good and both the smoothing and the centered derivative procedures are kept to calculate $e_2(d)$ and $D(d,t)$ from the measurement.

Finally an example of multi-scale analysis is performed on a simulated ligament subject to a capillary instability. The simulation uses the code from Ménard et al. (2007). The Navier-Stokes equations are coupled with the Level Set method to treat the interface motion and the ghost fluid approach is used to take into account jump conditions through the interface. The simulation is performed in 2D axisymmetric and half of the initial wave length is computed. The simulation code was validated with the results of the Rayleigh theory (Ménard et al., 2007). In the present application, the liquid is water and the ligament initial diameter is $D_L = 667 \mu\text{m}$. This corresponds to an Ohnesorge number $Oh = 4.6 \cdot 10^{-3}$ and a characteristic capillary time $t_\sigma = 2 \text{ ms}$. The initial perturbation is defined by its non-dimensionalized perturbation wavenumber $k = \pi D_L / \lambda = 0.524$ and its initial amplitude is $\eta_0 = 1.6 \text{ nm}$ ($\eta_0 / D_L = 2.46 \cdot 10^{-6}$).

Figure 8 shows the temporal evolution of the ligament. For the present operating conditions and in agreement with Ashgriz and Mashayek (1995), the ligament produces one main drop and a secondary ligament per perturbation wavelength. The calculation time was not long enough to see whether the secondary ligament will produce one or more satellite droplets. The $E_2(d,t)$ function was measured on the images according to

the procedure described above and the scale distributions $e_2(d,t)$ and scale diameters $D(d,t)$ were calculated. For several scales, Fig. 9 shows the temporal evolution of the scale diameter $D(d,t)$. For $t \in [0; 9 \text{ ms}]$, $D(d,t)$ is constant and is equal to D_L for all scales. The ligament remains non-deformed by the capillary instability during this time interval and keeps its cylindrical shape, which, in 2D, is a rectangle. As noticed in Eq. (8), for such a shape, the scale diameter is independent of the scale. In the time interval $t \in [9 \text{ ms}; 18 \text{ ms}]$, $D(d,t)$ increases for large scales and remains constant for small scales. The increase is sooner when the scale is greater. This shows that the ligament deformation imposed by the capillary instability is perceived by a scale interval that is a function of time. The increase of $D(d,t)$ for the large scales says that they perceive the ligament deformation as contraction. Note that the behavior found here agrees with Eq. (10): the scale diameter temporal derivative is positive for large scales and near zero for small scales. Finally, for $t \in [18 \text{ } \mu\text{m}; 22 \text{ } \mu\text{m}]$, $D(d,t)$ continues increasing for the large scales whereas it decreases for small ones. According to Eq. (8), this decrease announces that small scales perceive an elongation mechanism. In Fig. 8, we see that the contraction due to the main drop production induces a stretching of a secondary ligament on each side of the drop. The diameter of this secondary ligament is smaller than the initial ligament diameter and decreases with time. Therefore, its evolution is carried by the small scales only. This mechanism is the one described by the decrease of $D(d,t)$ at the small scales. As said above, this example shows that the temporal evolution of the scale diameter allows identifying the effective mechanisms in an atomization process. Furthermore, it provides a different way of describing and characterizing this process.

4. Results and Analysis

Figure 10 shows typical temporal evolutions of the scale distribution $e_2(d,t)$ for the LA1 and LC3 ligaments (these ligaments are shown in Fig. 4). As evoked in the previous section, the scale distribution in the scale space is a monotonously decreasing function since the perimeter of the eroded system always decreases as the scale d increases. The two graphs reveal an important difference between the liquids. For the high surface tension liquid (LA), the scale distribution temporal variation is slight but concerns the whole scale range. For the low surface tension liquid, the scale distribution temporal variation is large but concerns the small scale range only and more specifically the scale $d = 0$. Remembering that for $d = 0$ the scale distribution is a measurement of the system interface length, this difference reveals a more efficient atomization process in terms of interface production with the low surface tension liquid. Globally speaking, this result is not surprising since the surface tension is known to act against interface increase. Therefore, its opposition to surface production should diminish when it decreases.

Comparisons of the three ligaments of the same liquid are shown in Fig. 11 for liquids A and C and at the initial and final times only. The distributions shown in these graphs are reduced scale-distributions with no dimension. They are defined by:

$$e_2(d,t)D(0,t) = \frac{e_2(d,t)}{e_2(0,t)} = f\left(\frac{d}{D(0,t)}\right) \quad (15)$$

where $D(0,t)$ is the scale-diameter defined by Eq. (4). Several notable results appear from this representation. Although the ligaments of the same liquid do not have the same scale distributions (result not shown here), the initial and final reduced scale-distributions are very much alike. This result suggests that, with this injector, ligaments

of a given liquid follow similar behaviors of production and atomization. These behaviors are functions of the liquid since the initial and final reduced scale-distributions depend on the liquid. The initial reduced scale-distribution is wider for the low surface tension liquid. The shape of the final reduced scale-distributions changes with the liquid. (The reduced scale-distributions for the medium surface tension liquid lie between those obtained for the two other liquids.) For liquid A, the final scale-distributions are linearly scale dependent. Such distributions characterize sets of circles with the same diameter (see Fig. 7 for instance). In the present case this diameter is of the order of $2D(0,t_f)$ (see Fig. 11). To the contrary, the liquid C final reduced scale-distribution is typical of sets of circles with different diameters. This difference is due to the higher rate of small drop production observed in Fig. 4 for LC. It appears therefore that the scale distribution is very sensitive to small drop production. Finally, considering the small number of droplets produced per ligament, a measurement of a diameter distribution would not have been appropriate to quantify their size dispersion. To the contrary, the accuracy of the scale-distribution is not subjected to any statistical constraint.

The temporal evolutions of the scale-diameters of ligaments LA1 and LC3 are presented in Fig. 12 for several scales. The results for the other ligaments are similar. The scale-diameter temporal evolution depends on the scale d . Globally speaking, two regions can be identified, i.e., region 1 corresponding to $t < 200 \mu\text{s}$ for which $D(0,t)$ decreases, and region 2 corresponding to $t > 200 \mu\text{s}$ for which $D(0,t)$ remains constant or increases according to the situation. These two regions actually correspond to the regions of ligament deformation and ligament breakup, respectively.

The decrease of $D(d,t)$ for the small scales in region 1 is scale dependent. Considering the basic mechanism analysis presented in the previous section, this evolution indicates that the deformation of the ligament is perceived at these scales as an elongation mechanism whose rate (slope of the curves shown in Fig. 12) is scale dependent. At the same time, for the medium scales (around $100\ \mu\text{m}$), $D(d,t)$ increases in a scale dependent way. Therefore, the deformation of the ligament is perceived at these scales as capillary deformation (see results of the previous section).

This first observation reveals that the evolution of the ligament shapes is characterized by several concomitant mechanisms according to the scale of observation. Such a concomitancy is also visible on the simulated ligament results shown in Fig. 9. This concomitancy is linked to the fact that the scale-diameter function is an average information. Every structure developing on a ligament induces its own scale-diameter variation and the scale-diameter evolution of the whole system is an average of each structure contribution. In other words, for a given scale, the mechanism identified by the scale-diameter evolution corresponds to the averaged perception at this scale of the whole system shape variation. The mechanism concomitancy is the way the multi-scale approach describes and characterizes the atomization process.

In region 2, the scale-diameter at medium scales ($\sim 100\ \mu\text{m}$ and above) slightly decreases with time in a scale-dependent way. These scales are carried by the large droplet production process only. We learn here that this process is perceived as an elongation mechanism by medium and large scales. As noted in Fig. 9, this behavior is highly scale dependent.

In the same region, the scale-diameter at small scales is almost constant for liquid A and increases for liquid C (see Fig. 12). (The result for Liquid B is similar as the one of

Liquid C.) These behaviors indicate that, in average, a capillary deformation and breakup mechanism is perceived at small scales for liquid A, whereas a relaxation mechanism is perceived at these scales for liquid C. We see here that the scale-diameter evolution allows identifying the mechanisms that operate during the ligament breakup stage. In particular, the relaxation mechanism responsible for the small drop production and the enlargement of the drop-size distribution for liquids B and C is well observable. Therefore, despite this mechanism concerns a small amount of liquid, the scale-diameter at small scales appears very sensitive to it. This is because the variation of the whole system interface length is mainly due to the production and rupture of the secondary ligaments and that this information concentrates in the small scales.

From a more general point of view, these results say that the Rayleigh instability (capillary deformation and breakup mechanism) is described as a large scale process: it is controlled by the large scale of the system, and the perception in the whole scale range is imposed by what happens at this large scale. In other words, the variation of the scale-diameter at every scale is imposed by a single mechanism that depends on a single large scale. It is interesting to note that in the 2D description presented here, this large-scale controlled mechanism is associated to rather constant small-scale scale-diameters. No specific information concerns the small scales. However, when the Rayleigh mechanism combines with the production and the breakup of secondary ligaments (named here relaxation mechanism) the variation of the scale-diameter in the small scale range becomes independent of what happens in the large scale range and is imposed by the relaxation mechanism itself. (This behavior is also clearly observed in Fig. 9 for the simulated ligament.) We see here that this mechanism has a tremendous influence on the scale distribution in the small scale region (see Fig. 10). However, what happens at

small scales influences the large scales. Indeed, the production of secondary ligaments is possible if some liquid is extracted from the structures between which these ligaments develop. Thus, this mechanism reduces the potential increase of the large structures during the whole process. This explains why in Fig. 8 no variation of $e_2(d,t)$ is observed at large scale for the ligament LC3 whereas a clear increase of this function is observed for ligament LA1.

The temporal evolution of the scale-diameter can be associated to an evolution-rate $\alpha(d,t)$ defined by:

$$\alpha(d,t) = -\frac{1}{D(d,t)} \frac{dD(d,t)}{dt} \quad (16)$$

This function corresponds to the opposite of the local slopes of the curves shown in Fig. 12. At initial and final times, the logarithm of the scale-diameter $D(0,t)$ evolves linearly with time (see the dash lines in Fig. 12). These behaviors correspond to constant evolution-rates. For $d = 0$, the constant initial and final evolution-rates are noted $\alpha_i(0)$ and $\alpha_f(0)$, respectively.

At initial times, i.e., just after their production, the ligaments are subject to an elongation constraint. The evolution-rate $\alpha_i(0)$ is a characteristic of this constraint that is imposed by the dynamic of the liquid flow from which the ligaments are produced. As shown in Fig. 2, this flow has the shape of a triangular sheet and therefore has a spanwise or lateral component of velocity. This velocity subsists in the ligament causing its elongation. Since the initial perturbations of the liquid sheet vary with time, the

ligament formation process is not stationary. In consequence, the ligaments are different in size, in shape and have a different initial elongation rate $\alpha_i(0)$. This point is illustrated in Fig. 13 where $\alpha_i(0)$ is plotted as a function of the initial flow Weber number We_L defined by:

$$We_L = \frac{\rho_L V_q^2 D(0, t_i)}{\sigma} \quad (17)$$

(The velocity V_q is the mass flux average velocity equal to 7 m/s for all liquids.) We see in Fig. 13 that the initial elongation-rate varies from one ligament to another even for ligaments of the same liquid. Besides the reason exposed above, we should add here that $\alpha_i(0)$ might slightly depends on the ligament identification procedure described in Fig. 3. However, despite a non-negligible scatter of the points in Fig. 13, we see that, in average, $\alpha_i(0)$ increases with We_L , i.e., when the surface tension decreases. This is due to the fact that a low surface tension liquid plays less against surface variation per elongation. As far as the initial elongation process is concerned, we see in Fig. 12 that it lasts longer when the surface tension is low. This is due to the fact that surface tension pressure becomes effective for smaller ligament diameter when the surface tension is low. This low level of diameter is reached thanks to the elongation mechanism. The inverse of the initial variation-rate gives a characteristic time t_e of the initial elongation mechanism:

$$t_e = \frac{1}{\alpha_i(0)} \quad (18)$$

Besides the elongation mechanism, the initial ligaments are also subject to capillary deformation that depends on the initial ligament shape. A characteristic time t_σ of this mechanism is given by:

$$t_\sigma = \sqrt{\frac{\rho_L D(0, t_i)^3}{\sigma}} \quad (19)$$

The behavior of the ligaments should depend on the ratio of the capillary characteristic time on the elongation characteristic time (Frankel and Weihs, 1985; Marmottant and Villiermaux, 2004b). This ratio introduces a new Weber number $We(t_i)$, i.e.:

$$We(t_i) = \left(\frac{t_\sigma}{t_e}\right)^2 = \frac{\rho_L D(0, t_i)^3 \alpha_i(0)^2}{\sigma} \quad (20)$$

Figure 14 shows the final variation-rate $\alpha_f(0)$ as a function of $We(t_i)$ for the nine ligaments investigated here. It shows that $\alpha_f(0)$ decreases when $We(t_i)$ increases and that all results roughly organize as a single behavior. This result demonstrates a strong correlation between the ligament initial conditions in terms of elongation contribution and the final breakup stage. From Fig. 14, a critical Weber number We_C appears: it segregates ligaments according to the sign of the final evolution-rate $\alpha_f(0)$. We_C is of the order to 0.03, i.e. $t_\sigma/t_e = 0.17$. Two situations occur.

When $We(t_i) < We_C$, i.e., when t_σ is much lower than t_e , $\alpha_f(0) > 0$: The elongation has a moderate influence on the ligament evolution. The drop production is controlled by the

capillary breakup mechanism and the drops produced have equivalent size. High surface tension ligaments preferentially adopt this mechanism.

When $We(t_i) > We_C$, i.e., when t_σ is larger than $0.2t_{e,}$, $\alpha_l(0) < 0$: The initial elongation mechanism has a consistent influence on the ligament evolution. In particular, it enhances the production of secondary ligaments. Therefore, the drop production combines capillary and relaxation mechanisms. The capillary mechanism acts on the large ligament portions and produces the large droplets whereas the relaxation mechanism acts on the secondary ligaments and produces the small drop population. In other words, the atomization process cascades in the scale space, which results in a larger drop-size distribution. Low surface tension liquid ligaments with a sufficient initial elongation adopt this mechanism.

For three ligaments (LA1, LB2 and LC3), Fig. 15 shows the temporal evolution of the function $\beta(d,t)$ for $d = 0$. At small times, $\beta(0,t)$ increases and reaches a maximum. (For liquid A, this variation is not very much pronounced.) This behavior is related to the initial period where the elongation mechanism is active. We see here that surface variation rate increases when the surface tension decreases. Furthermore, in agreement with the observation made in Fig. 12, we see that the elongation mechanism lasts longer when the surface tension decreases. After the maximum, $\beta(0,t)$ decreases. This behavior corresponds to the ligament breakup region. Once again, the variation of $\beta(0,t)$ for liquid A in this region is not very much pronounced. However, the evolution rate of $\beta(0,t)$ strongly decreases as the surface tension decreases. Furthermore, we note that, whereas $\beta(0,t)$ remains positive for liquid A, it reaches negative values for liquids B and C. For liquid A, the breakup is associated to a positive slightly decreasing surface

variation rate. For liquids B and C, the breakup is associated to a sharp decreasing surface variation rate and the final negative values say that the relaxation mechanism actually reduces the amount of interface created during the elongation period. Despite this, the total surface production remains better than with liquid A. A similar behavior has been recently identified on the breakup process of a drop interacting with a turbulent field (Andersson and Helmi, 2014). It actually says that the fragmentation requires more energy than the one expressed by the final surface-energy balance.

This work ends with a specific analysis of the final scale-distributions, i.e., those representing the droplets issued from the atomization of the ligaments. In their investigation dedicated to stretched ligaments, Marmottant and Villermaux (2004b) found that the gamma distribution (Eq. (12)) well fitted the drop diameter distribution. Following the mathematical development presented in a previous work (Dumouchel et al. 2008), we can demonstrate that the scale distribution of a set of spheres whose diameters are distributed according to Eq. (12) is:

$$e_2(d) = \frac{2\nu}{D_{10}} \frac{\Gamma\left(\nu + 1, \frac{\nu d}{D_{10}}\right) - \frac{\nu d}{D_{10}} \Gamma\left(\nu, \frac{\nu d}{D_{10}}\right)}{\Gamma(\nu + 2)} \quad (21)$$

where $\Gamma(x,y)$ represents the incomplete gamma function. The couples of parameters (ν, D_{10}) that offers the best fit between the measured and the mathematical scale-distributions are determined thanks to a Scilab routine written for this purpose. Three examples of fit are presented in Fig. 16. We see that the agreement between the mathematical function and the measurements is good in the small and large scale

regions and acceptable for the medium scale region. (Similar quality was obtained for the other ligaments.) The mathematical diameter distribution does not represent the diameters of the produced drops but those of the set of circular elements that has the same surface-scale distribution as the one measured. As explained when introducing the scale distribution in Section 3, different systems may report the same scale distribution. Such systems are seen as equivalent systems.

For the nine ligaments, Figure 17 displays the order ν as a function of the Weber number $We(t_i)$ (Eq. (20)). A clear correlation appears, i.e.:

$$\nu \propto \frac{1}{We(t_i)} \quad (22)$$

The decrease of the order ν with $We(t_i)$ illustrates the widening of the equivalent system drop diameter distribution when the surface tension decreases. As far as the parameter D_{10} is concerned, Fig. 18 shows that it is proportional to the scale-diameter $D(0,t_i)$. For the high surface tension liquid we have $D_{10}/D(0,t_i) = 1.7$ which is quite near the 1.89 coefficient of the Rayleigh. The two other liquids report the same constant of proportionality: $D_{10}/D(0,t_i) = 1.26$. This lowest value highlights a more efficient atomization mechanism in terms of interface production.

5. Conclusion

The temporal multi-scale description of the ligaments produced by the atomization of liquid sheets issuing from triple-disk nozzle allows identifying the mechanisms responsible for their evolution. When produced, the ligaments have different shapes, thickness and length. At initial times, they are subjected to two mechanisms, i.e.,

elongation and capillary deformation. The elongation component is a reminiscence of the dynamic of the sheet from which the ligaments emanate. At breakup time, the drop production results from the capillary breakup and the relaxation mechanisms. The first one produces large drops whereas the second one produces small droplets. The relaxation mechanism takes place on secondary stretched ligaments whose presence is found to be correlated to a Weber number based on the initial ligament elongation rate and diameter, and the liquid surface tension. A critical value We_C of this number is reported, i.e., $We_C = 0.03$. For ligaments with a Weber number less than We_C the effect of initial elongation is limited and no secondary ligaments are produced. The subsequent breakup process involves the capillary mechanism only and drops of equivalent size are produced. For ligaments with a Weber number greater than We_C , the initial elongation favors the development of secondary stretched ligaments. The subsequent breakup process involves the capillary and relaxation mechanisms and the droplets show various diameters. In this case, it is found that the energy involved in the fragmentation process is greater than the final surface energy balance.

These results say that when the surface tension decreases, the ligament atomization process cascades in the scale space and the drop set has a different topology. This behavior is conditioned by the presence of an elongation constraint when the ligament is produced. In the context of liquid atomization, this is always the case since the production of ligaments intends to oppose interface growths imposed by stretch constraints. Two effects of the surface tension enter in the explanation of this behavior, i.e., the surface tension influences both the scale at which capillary forces are effective and the production of interface by any elongation constraint.

Finally, the scale-distributions characterizing the droplets have been satisfactorily reproduced by a mathematical distribution derived from the drop-diameter distribution issuing from the fragmentation model due to Marmottant and Villermaux (2004a). This drop-diameter distribution characterizes the set of spheres that has the same scale-distribution as the one measured. The mathematical distribution introduces two parameters that correlate with the ligament initial Weber number and size.

As far as the analytical side is concerned, this work demonstrates that the multi-scale analysis has a high potential to investigate liquid atomization process. It allows analyzing real temporal evolution of a single element without any drawback of statistical representation provided that the spatial resolution is high enough. This condition is required in order to have a sufficiently wide range of analyzing scales. The notion of scale-diameter introduced in this work appears appropriate to analyze the system shape temporal evolution. The temporal variation of the scale-diameter defines the average perception at a given scale of the shape variation of the whole system. It is found here, that several mechanisms are perceived at the same time at different scales. This concomitancy is a characteristic of the investigated atomization process.

Acknowledgments

The authors acknowledge the financial support from the French National Research Agency (ANR) through the program Investissements d'Avenir (ANR-10 LABX-09-01), LABEX EMC3.

References

- Andersson, R., Helmi, A., 2014. Computational fluid dynamics simulation of fluid particle fragmentation in turbulent flows. *Applied Math. Mod.* 38:4186-4196
- Ashgriz, N., Mashayek, F., 1995. Temporal analysis of capillary jet breakup. *JFM* 291: 163-190
- Brémond, N., Villermaux, E., 2006. Atomization by jet impact. *JFM* 549:273-306
- Clanet, C., Villermaux, E., 2002. Life of a smooth liquid sheet. *JFM* 462:307-340
- Dumouchel, C., 2008. On the experimental investigation on primary atomization of liquid streams. *Exp. In Fluids* 45, 371-422
- Dumouchel, C., Blaisot, J.B., 2013. Multi-scale analysis of liquid atomization Processes and Sprays. ILASS – Europe 2013, Chania (Grèce) September 2013
- Dumouchel, C., Cousin, J., Grout, S., 2008. Analysis of two-dimensional liquid spray images: The surface-based scale distribution. *Journ. Flow Visu. Image Proc.*, 15: 59-83
- Dumouchel, C., Cousin, J., Triballier, K., 2005a. On the role of the liquid flow characteristics on low-Weber number atomization processes. *Exp. In Fluids*, 38, 637-647
- Dumouchel, C., Cousin, J., Triballier, K., 2005b. Experimental analysis of liquid-gas interface at low Weber number: Interface length and fractal dimension. *Exp. In Fluids*, 39, 651-666
- Dumouchel, C., Grout, S., 2009. Application of the scale entropy diffusion model to describe a liquid atomization process. *Int. Journal of Multiphase Flow*, 35, 952-962

- Fdida, N., Blaisot, J.B., 2010. Drop size distribution measured by imaging: determination of the measurement volume by the calibration of the point spread function. *Meas. Sci. Technol.*, 21, 025501 (15p)
- Frankel, I., Weihs, D., 1985. Stability of a capillary jet with linearly increasing axial velocity (with application to shaped charged). *JFM* 155, 289-307
- Frankel, I., Weihs, D., 1987. Influence of viscosity on the capillary instability of a stretching jet. *JFM* 185, 361-383
- Fraser, R.P., Eisenklam, P., Dombrowski, N., Hasson, D., 1962. Drop formation from rapidly moving liquid sheet. *A.I.Ch.E. Journ.*, 8, 672-680
- Lozano, A., Call, C.J., Dopazo, C., Gacia-Olivares, A., 1996. Experimental and numerical study of the atomization of a planar liquid sheet, *Atomization and Sprays* 6, 77-94
- Marmottant, P., Villermaux, E., 2004a. On spray formation. *JFM* 498, 73-111
- Marmottant, P., Villermaux E., 2004b. Fragmentations of stretched liquid ligaments. *Phys. of Fluids*, 16, 2732-2741
- Ménard, T., Tanguy, S., Berlemont, A., 2007. Coupling Level Set/VOF/ghost Fluid methods : Validation and application to 3D simulation of primary break-up of liquid jet. *Int. Journal of Multiphase Flow*, 33, 510-524
- Mugele, A., Evans, H.D., 1951. Droplet size distribution in sprays. *Ind. Engng. Chem.* 43, 1317-1324
- Pimbley, W.T., Lee, H.C., 1977. Satellite droplet formation in a liquid jet. *J. Res. Develop.* 21-30, January 1977
- Rayleigh, L., 1878. On the instability of jets. *Proc. Lond. Math Soc.* 10, 4-13

- Rutland, D.F., Jameson, G.J., 1971. A non-linear effect in the capillary instability of liquid jets. *JFM* 46, 267-271
- Sindayihebura, D., Dumouchel, C., 2001, Pressure atomizer: Hole break-up of the sheet. *Journ. Visualisation* 4: 5
- Tong, A.Y., Wang, Z., 2007, Relaxation dynamics of a free elongated liquid ligament. *Phys. of Fluids* 19, 092101 (1-11)
- Yuen, M.C., 1968. Non-linear capillary instability of a liquid jet. *JFM* 33: 151-163

Table and Figure captions

Table 1: Dimensions of the triple-disk nozzle (all dimensions are given in μm)

Table 2: Physical properties of the liquids (percentage indicates a proportion in weight)

Figure 1: The triple disk nozzle

Figure 2: Shadowgraph image of the liquid flow issuing from the triple-disk nozzle at 0.1 MPa (Liquid: Water, Visualized field: 7.5 mm x 11.3 mm)

Figure 3: Example of an atomizing ligament (LC)

Figure 4: Temporal sequences for LA1 (left, time gap = 40 μs), LB2 (center, time gap = 80 μs) and LC3 (right, time gap = 40 μs)

Figure 5: a) System of any shape. Surface = S_T , b) Erosion of the system with a circular structuring element of diameter d . The surface $S(d)$ of the remaining part of the system is the white surface delimited by the dashed line.

Figure 6: Initial and final stages of the 2D representation of the three basic mechanisms

Figure 7: Measured and theoretical scale distributions obtained for the synthetic image system

Figure 8: Simulation of a ligament subject to a capillary instability

Figure 9: Temporal evolution of the scale diameters of the simulated ligament shown in Fig. 8

Figure 10: Temporal evolution of the scale distribution $e_2(d,t)$ (left: LA1; right: LC3. These ligaments are shown in Fig. 4)

- Figure 11:** Initial and final reduced scale-distributions. Comparison of the ligaments of a same liquid (from top left to bottom right: LA at initial time, LC at initial time, LA at final time, LC at final time)
- Figure 12:** Temporal evolution of the scale-diameter for several scales (left: LA1; right: LC3, same scale for both graphs)
- Figure 13:** Initial elongation rate $\alpha_i(0)$ at scale $d = 0$ as a function of the Weber number We_L (given by Eq. (13))
- Figure 14:** Final elongation rate $\alpha_f(0)$ at scale $d = 0$ as a function of the Weber number $We(t_i)$ (given by Eq. (16))
- Figure 15:** Temporal evolution of the function $\beta(0,t)$ for ligaments LA1, LB2 and LC3
- Figure 16:** Comparison between measured and mathematical scale-distribution at final time (LA1, LB2 and LC3)
- Figure 17:** Correlation between the order ν and the Weber number $We(t_i)$
- Figure 18:** Correlation between the parameter D_{10} and initial scale-diameter $D(0,t_i)$

Fig. 1

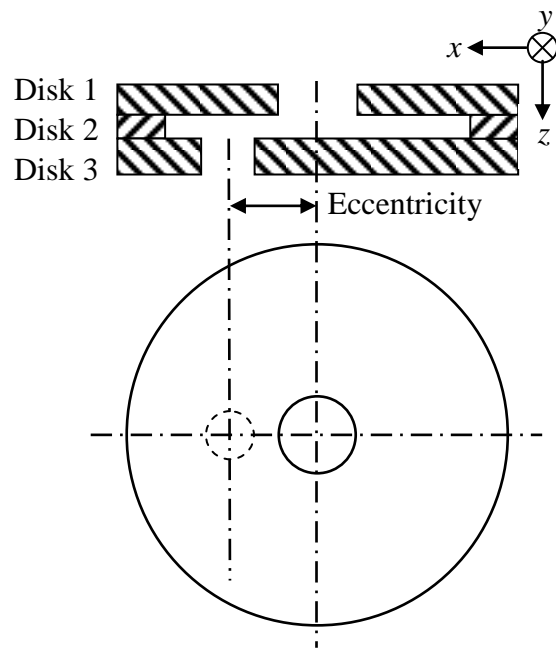


Fig. 2

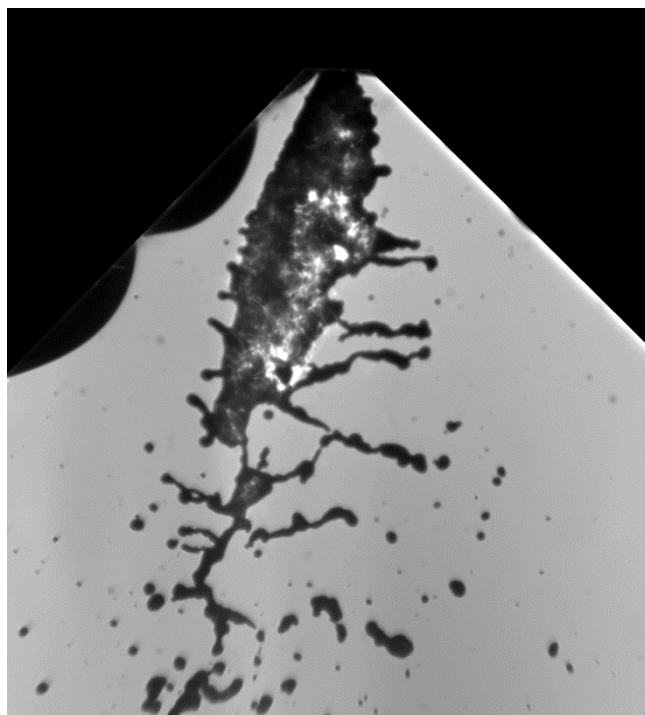


Fig. 3

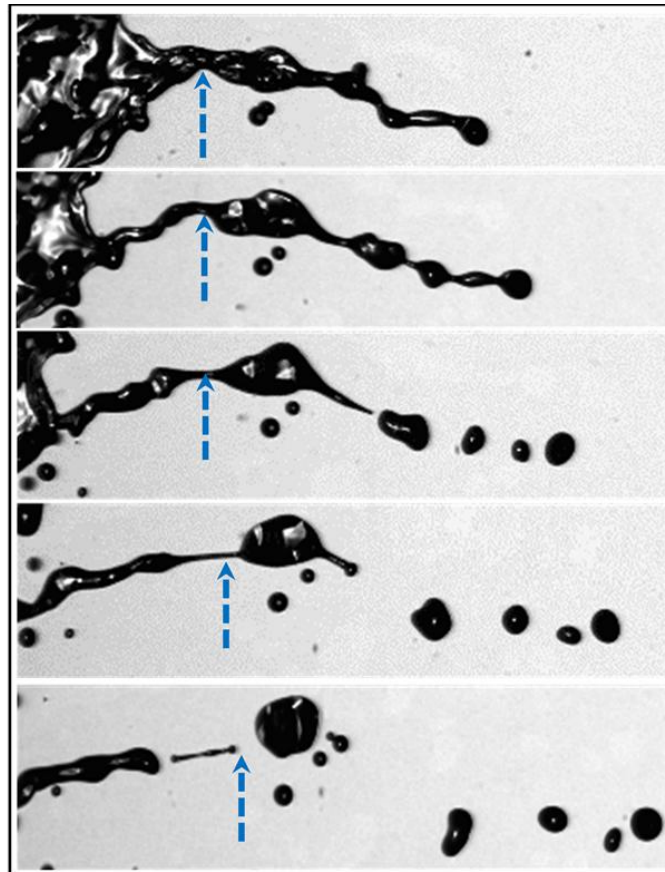


Fig. 4

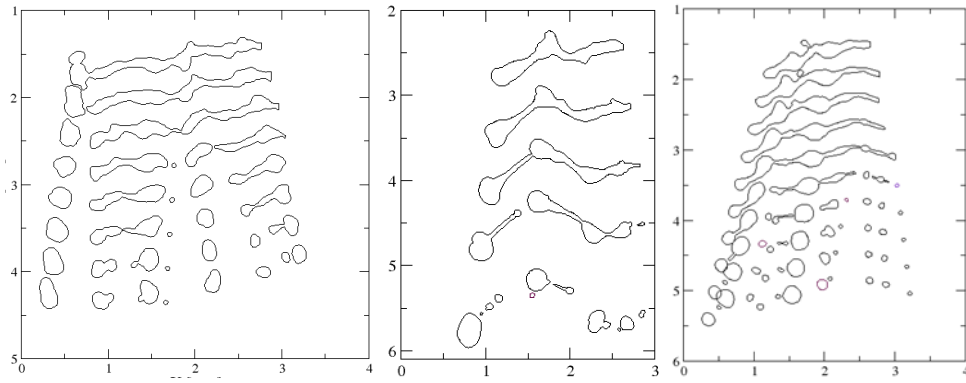


Fig. 5

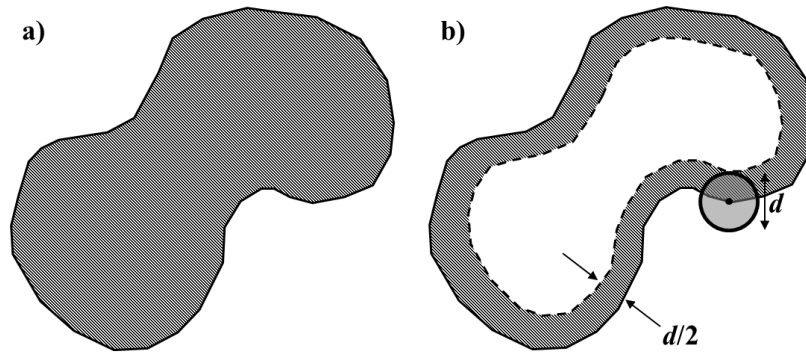


Fig. 6

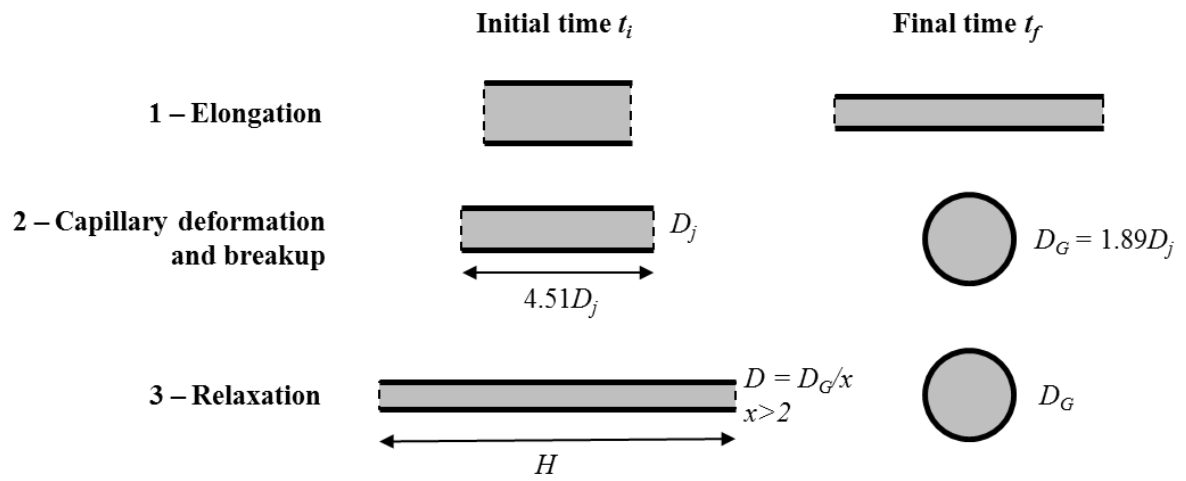


Fig. 7

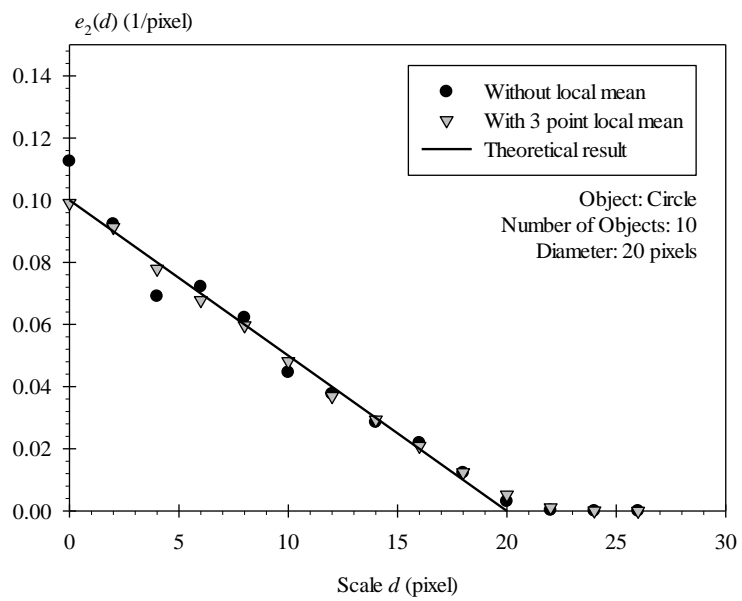


Fig. 8

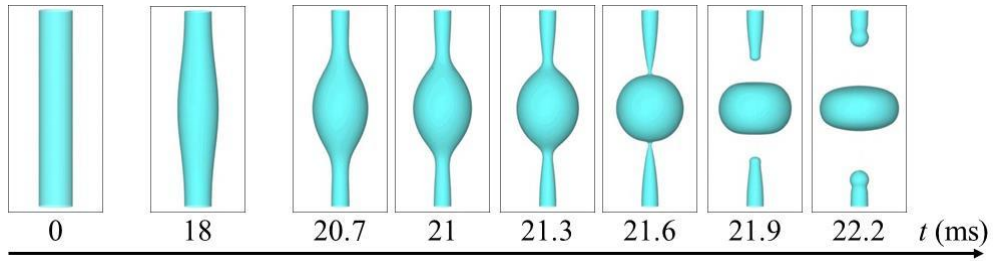


Fig. 9

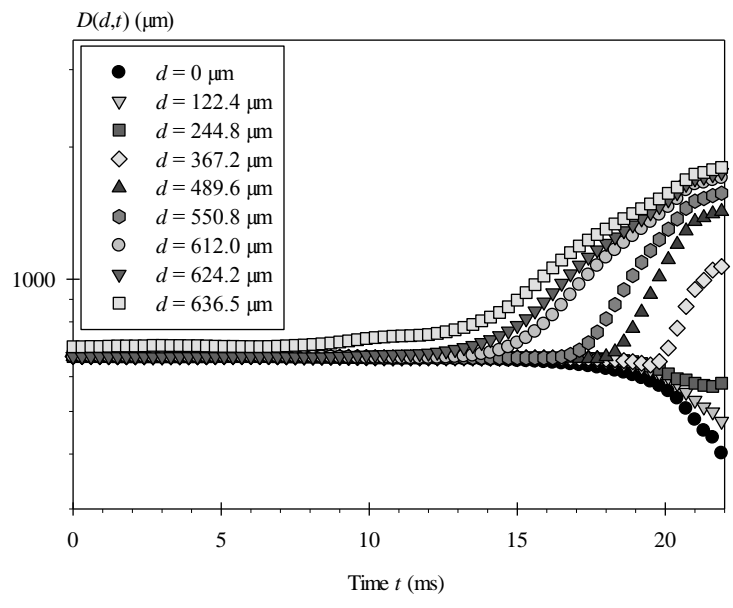


Fig. 10

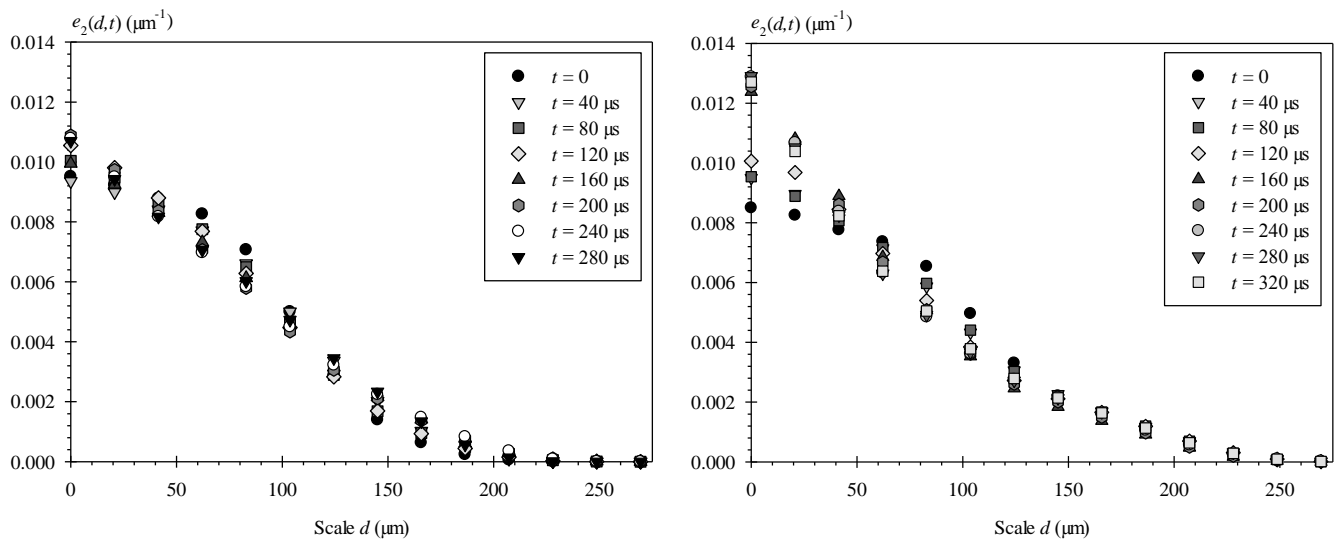


Fig. 11

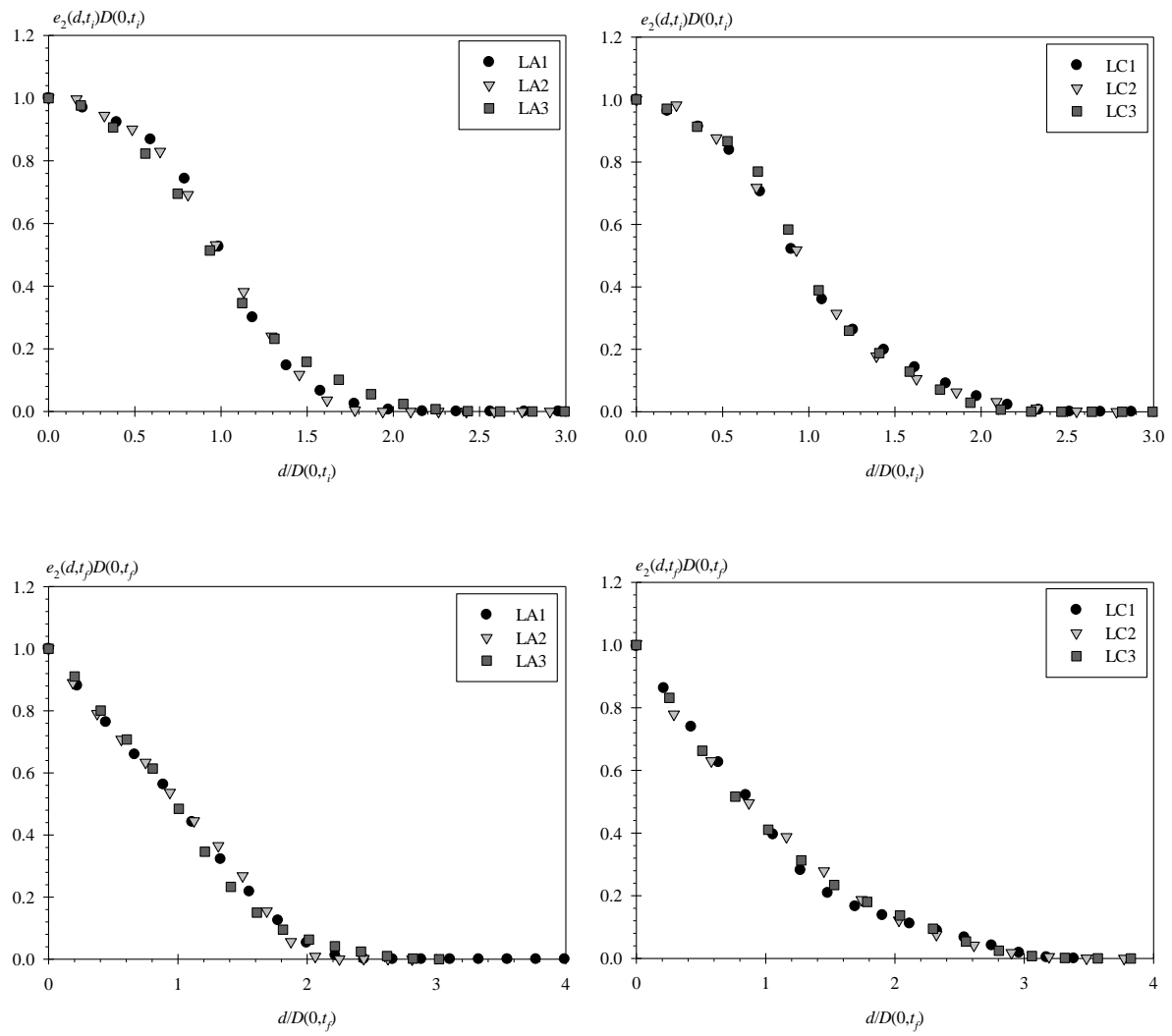


Fig. 12

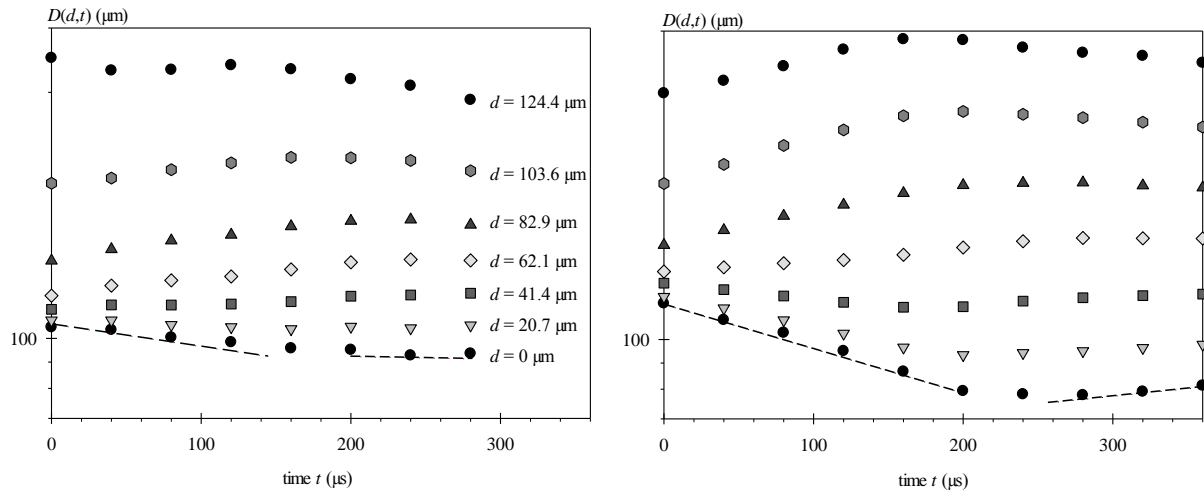


Fig. 13

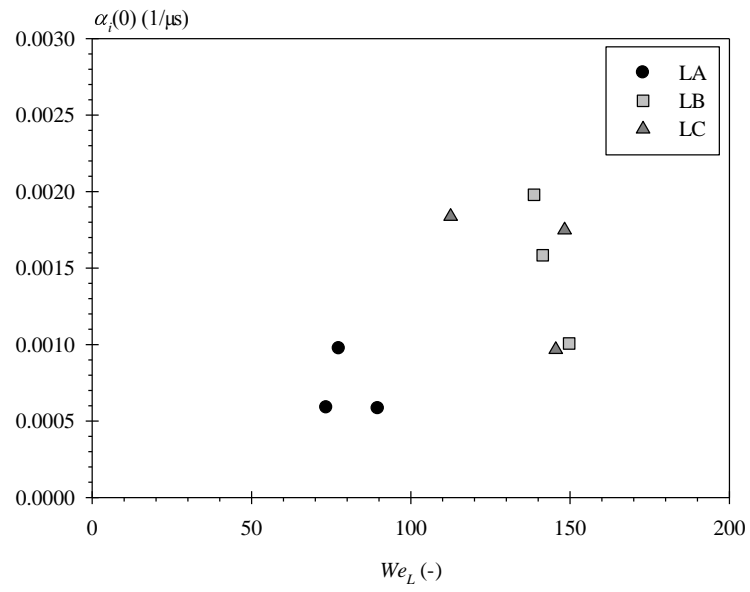


Fig. 14

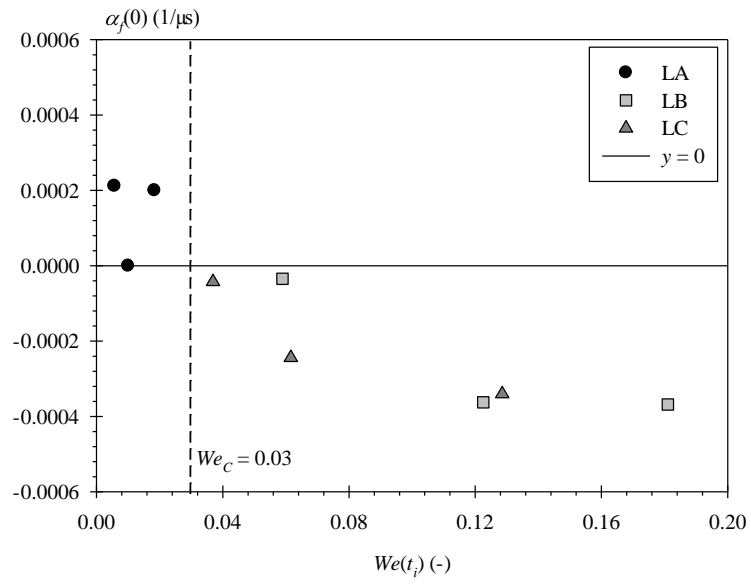


Fig. 15

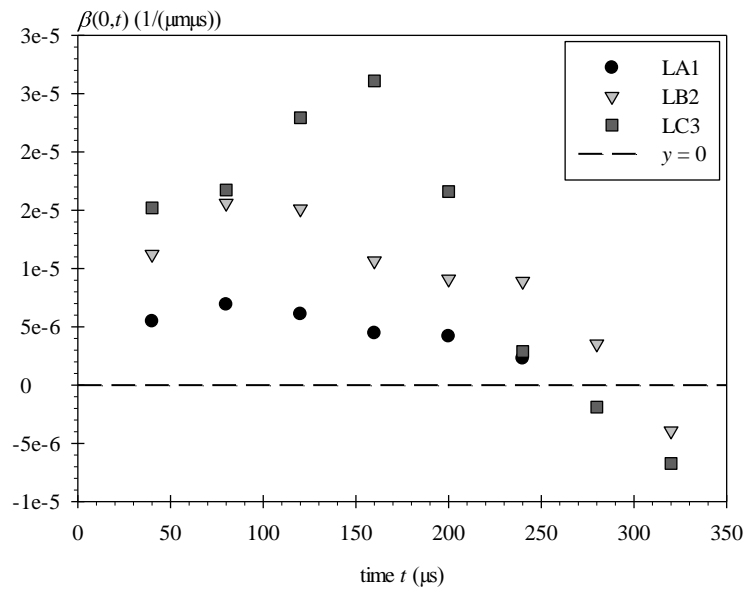


Fig. 16

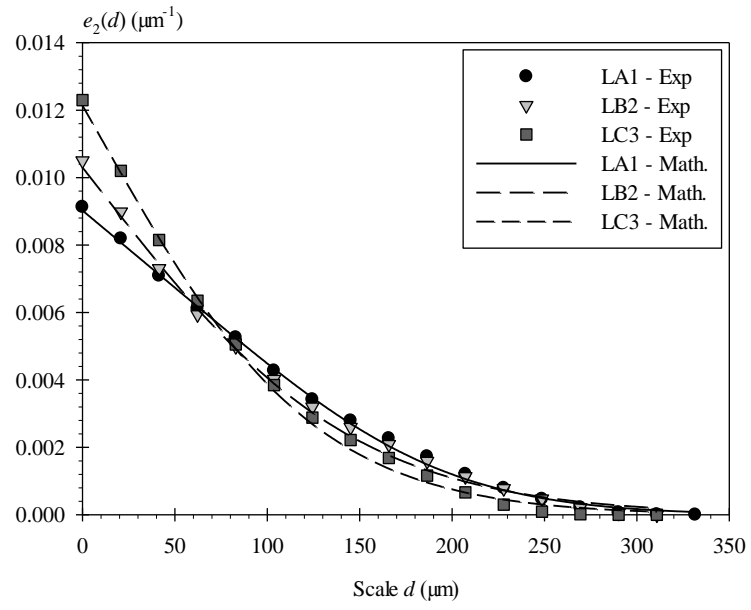


Fig. 17

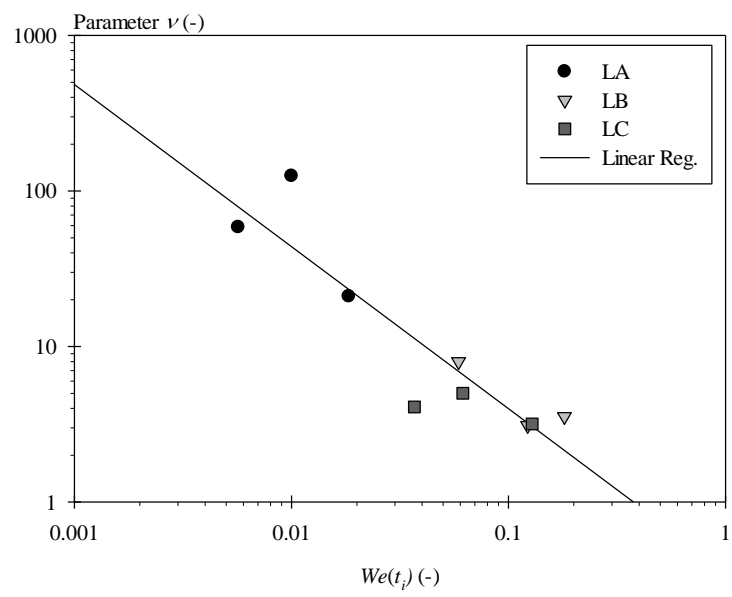


Fig. 18

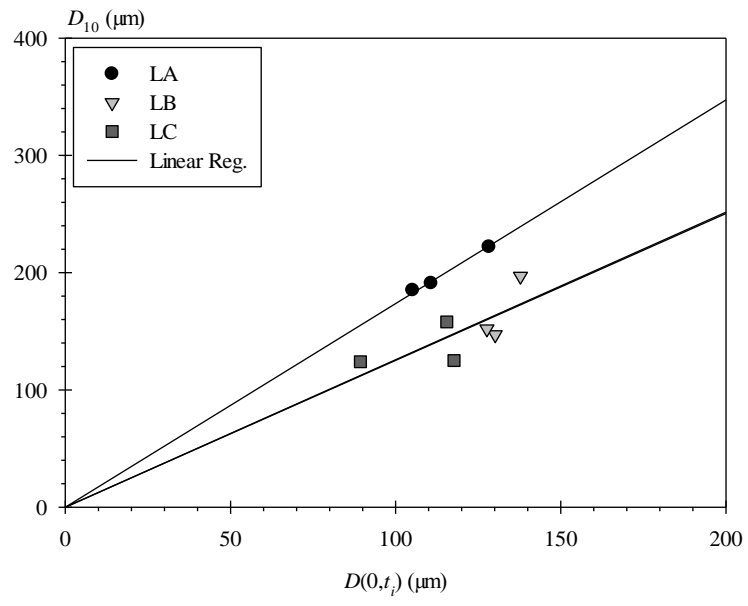


Table 1

Nozzle dimension (μm)		
Disk 1	thickness	400
	Orifice diameter	600
Disk 2	thickness	100
	Orifice diameter	4510
Disk 3	thickness	150
	Orifice diameter	400
	Eccentricity	450

Table 2

Liquid	Density ρ_L (kg/m³)	Surface tension σ (N/m)	Dynamic viscosity μ_L (kg/(ms))
A - Water	994	0.070	$1 \cdot 10^{-3}$
B - Water-Ethanol 10%	973	0.044	$1.32 \cdot 10^{-3}$
C - Water-Ethanol 15%	967	0.038	$1.57 \cdot 10^{-3}$